Journal of Alloys and Compounds 648 (2015) 838–844

Contents lists available at ScienceDirect

Journal of Alloys and Compounds

journal homepage: http://www.elsevier.com/locate/jalcom

Femtosecond-pulse laser-ablation-induced synthesis and improved emission properties of ultrafine Y_2O_3:Er^{3+}, Yb^{3+} nanoparticles with reduced nonradiative relaxation

Changbin Zheng*, Guilong Yang, Kuo Zhang, Chunrui Wang, Hualong Wang, Fei Chen, Yang He

State Key Laboratory of Laser Interaction with Matter, Changchun Institute of Optics, Fine Mechanics, and Physics, Chinese Academy of Sciences, Changchun, 130033, PR China

ARTICLE INFO

Article history:
Received 13 April 2015
Received in revised form
27 June 2015
Accepted 29 June 2015
Available online 6 July 2015

Keywords:
Rare earth alloys and compounds
Laser ablation
Optical properties
Optical spectroscopy
Nonradiative relaxation

ABSTRACT

Nanomaterials with effective visible upconversion emission have received special attention due to the potential application in the fields including biological labeling, imaging, and photodynamic therapy. The main focus of this work is the improvement of the upconversion emission properties, which is enhanced emission intensity and prolonged decay time, by reducing nonradiative relaxation assisted by high energy phonon. Y_2O_3:Er^{3+}, Yb^{3+} nanoparticles (considerably < 50 nm) were directly prepared through femtosecond-pulse laser ablation conducted on the corresponding oxide mixture. It was observed that the number of carbonate and hydroxyl groups remaining in the nanoparticles was decreased. The upconversion and infrared emission properties of the particles were investigated using 976-nm continuous-wave laser radiation, and it was found that the relative red-to-green emission intensity decreased. The samples also exhibited higher integral intensity and reduced power dependence on the excitation intensity, which indicates a more effective upconversion process. The decay time for upconversion emission was lengthened, and for the first time (to the best of our knowledge), infrared emission at 1550 nm was almost suppressed. As a result of the elimination of the carbonate and hydroxyl groups, nonradiative relaxation assisted by high-energy phonons was reduced, thereby increasing the decay time and upconversion emission and decreasing the infrared emission.

1. Introduction

Visible upconversion (UC) rare-earth-doped nanomaterials have been investigated extensively for the development of biological labeling, imaging, and photodynamic therapy [1–6]. Compared to traditional labels, labels containing UC nanomaterials that are excited by near-infrared diode lasers have many advantages, such as reduced photodamage to living organisms, weaker background fluorescence, and a deeper detection range. Various methods have been developed for the preparation of oxide nanocrystals, which are used to produce UC nanomaterials, including sol–gel [7–12], co-precipitation [13–15], solution combustion [16,17], and hydrothermal method [18–21]. However, UC nanomaterials fabricated in this way typically have low emission efficiency and, thus, require more pump power than downconversion (DC) materials, which have limited practical applications in biolabeling [22].

As is well known, the nonradiative relaxation rate is a limiting factor in UC efficiency [15], and hydroxyl and carbonate groups with high phonon energy increase the probability of nonradiative relaxation; thus, they influence the emission properties considerably. The presence of these substances has been proven to be the primary energy-loss channel for doping ions, resulting in strong fluorescence quenching [23]. As the main sources of these high-energy phonon groups are the initial materials used during the preparation of UC nanomaterials, avoiding contamination during the preparation process is an important criterion for improving the UC efficiency and performance of the resultant nanomaterials. Efficiency improvements in visible UC emission have been realized in Pr^{3+}- and Yb^{3+}-doped Y_2O_3 nanoparticles prepared using the femtosecond-pulsed laser ablation method [24]. As this method helps prevent possible chemical contamination and, therefore,

* Corresponding author. Dong Nanhu Road 3888, Changchun, 130033, Jilin, PR China.
E-mail address: zhengchangbin@ciomp.ac.cn (C. Zheng).

http://dx.doi.org/10.1016/j.jallcom.2015.06.258
0925-8388/

reduces high-energy-phonon-assisted nonradiative relaxation, these nanoparticles exhibit high UC emission intensity.

The purpose of this study is to examine the influence of nonradiative emission on the emission characteristics of UC nanomaterials. Yttrium oxide is a common host material for rare earth ions with broad transparency range (0.2–8 μm), high chemical and structural stability and low phonon energy (about 600 cm^{-1}). An Er^{3+} ion is chosen as the active ion for this study, as these ions have high UC efficiency and abundant transition processes, and are therefore suitable for experiments investigating the effects of nonradiative relaxation on UC emission. The influence of a Yb^{3+} ion on the emission (as a sensitizer) is also investigated so as to better understand the interaction of high-energy phonons with active ions. Therefore, Y_2O_3:Er^{3+}, Yb^{3+} nanoparticles are prepared using femtosecond-pulse laser ablation conducted on the corresponding oxide mixture. The visible UC and near-infrared DC spectroscopic characterization of these nanoparticles are then shown, and compared with those prepared using commonly used sol–gel methods. The decay time and power dependence of the UC emission are measured, and the results are discussed in terms of an inferred nonradiative-relaxation.

2. Experimental procedures

2.1. Preparation of Y_2O_3:Er^{3+}, Yb^{3+} nanoparticles using femtosecond pulsed laser ablation

Y_2O_3 nanoparticles doped with 1 mol% Er^{3+} and 0 or 5 mol% Yb^{3+} were prepared using a laser ablation method, as previously reported [24]. Briefly, Y_2O_3, Er_2O_3, and Yb_2O_3 powders with 99.99% purity were mixed and pressed into pellets using a pressure of 10 MPa that was applied for 90 s. These pellets were used as targets for a Ti:sapphire femtosecond laser beam (Spectra Physics) operated at 800 nm and with a pulse width of 120 fs, repetition rate of 1 kHz, pulse energy of 0.8 mJ/pulse, and a diameter of 0.2 mm at the pellet surface. The pellets were mounted on a 2-D motorized translation stage, which drew parallel lines with 0.2-mm separation at a speed of 1.0 mm/s. The laser pulse was focused onto the pellet surfaces by a quartz lens at normal incidence. By scanning the incident beam on the target pellets, the target surface was modified in a very short time. Nanoparticles were then produced by redepositing the ablated plasma onto the target surface after the beam had passed.

2.2. TEM and FTIR characterization

The nanostructure was removed from the substrate surface with a blade and dispersed into alcohol through ultrasonic oscillation to form a suspension. A small drop of this suspension was then spread onto a copper mesh and covered with an amorphous carbon film for observation using high-resolution transmission electron microscopy (TEM, JEOL JEM-2010). The Fourier-transform infrared (FTIR) spectra were measured at room temperature using a Perkin–Elmer Spectrum One FTIR.

2.3. Photoluminescence characterization

The room-temperature UC emissions under 976-nm diode laser excitation were recorded using a monochromator (Zolix Instruments Co. Ltd.) and a photomultiplier tube (Hamamatsu CR131), with the beam being focused onto an area of 2 mm^2. Finally, the fluorescence decay times were measured using a digital-storage oscilloscope (Tektronix 5052) and the infrared DC spectra were detected by an InGaAs photodiode (Thorlabs DET 410/M). Note that the emission spectra were carefully measured under the same experimental conditions, and therefore, the Er^{3+} ion emission intensities could be compared directly.

2.4. Preparation of Y_2O_3:Er^{3+}, Yb^{3+} nanoparticles using sol–gel method

For comparison, another series of samples with equal doping concentrations were prepared using a typical sol–gel method, the fabrication process and characterization of which are given in Ref. [25]. Briefly, Y_2O_3, Er_2O_3 and Yb_2O_3 powders were dissolved in nitric acid. After the solution was dried, the corresponding nitrates were obtained. These nitrates with corresponding mole ratio of cations (100:1:0 or 10) were completely dissolved in deionized water. Subsequently, citric acid was added into the solution with a mole ration of cations to citric acid of 1:4. After complete dissolution, the pH of the solution was adjusted to 6.0 by addition of ammonium hydroxide. The solution was then dried at 120 °C for 24 h until it was transformed into a black bulk, which was further calcined at 800 °C for 2 h. Then, the powders were pressed to pellets using a pressure of 10 MPa that was applied for 90 s. The TEM micrograph of nanoparticles prepared using the same method has been present in Ref. [25]. The average diameter of these sol–gel nanoparticles was approximately 40 nm. These samples and those prepared through the laser ablation process will be henceforth referred to as the SG and LA samples, respectively.

3. Results and discussion

3.1. Structural and FTIR characterization

Fig. 1 shows the TEM image and the particles size distribution histogram of the particles prepared by laser ablation method. As seen in Fig. 1a, in the LA method preparation process, ultrafine nanoparticles with sizes considerably smaller than the measuring scale can be obtained. The mean particle diameter is about 10 nm and less than that of nanocrystals prepared by sol–gel method, which are shown in Ref. [25]. Fig. 2 shows the FTIR spectra of the Y_2O_3:Er^{3+}, Yb^{3+} nanoparticles prepared through the LA and SG methods. The band centered at approximately 3500 cm^{-1} was attributed to the characteristic vibration of the hydroxyl (OH^-) groups [19], while another band, centered at approximately 1500 cm^{-1}, was caused by the vibration of the carbonate (CO_3^{2-}) group [26]. From the spectra, it is apparent that the intensity of the OH^- and CO_3^{2-} groups was significantly decreased in the LA samples compared with the SG samples. It is commonly known that the groups are either absorbed from the environment, or introduced during the preparation process. Since that both series of samples are reserved under the same condition in the air and the LA samples have larger surface to volume ratio due to the smaller size, the LA samples should present stronger absorption intensity, if these groups were mainly absorbed from the air. Therefore, these groups are mainly arisen from the residues of the precursor, which are commonly found in sol-gel-prepared samples. The presence of these groups is inherent to the chemical precursor method and is one of the main unresolved issues in the synthesis [23]. The FTIR intensity tended to decrease with the increase of particle size [27]. Further annealing of the nanoparticles prepared by chemical method could reduce the number of these groups, but result in the growth and agglomeration [17,28], which is undesirable in the field of biological image. In contrast, because the laser-ablation preparation process does not use any organic precursor and, thus, avoids the introduction of any OH^- and CO_3^{2-} group residues to the system, the spectra indicate that the number of OH^- and CO_3^{2-} groups in the LA samples was smaller than that in the SG samples, despite of the smaller particle size. The significance of these groups in the

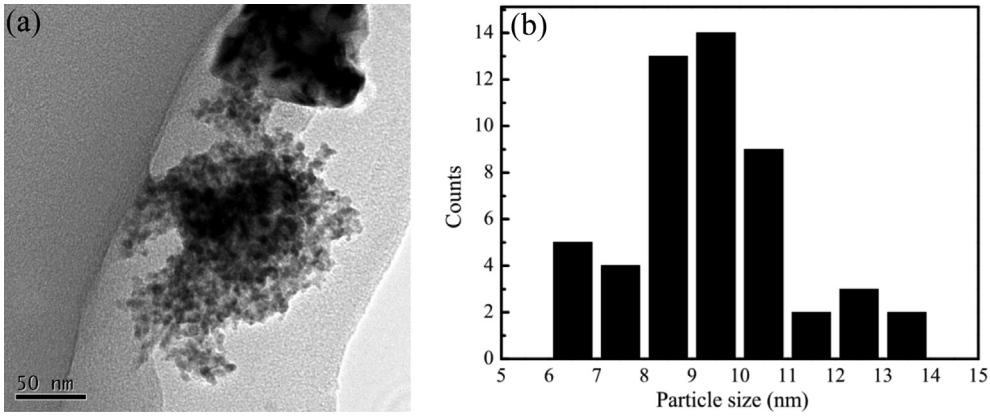

Fig. 1. Y_2O_3:Er^{3+}, Yb^{3+} nanoparticles. Transmission electron microscopy image (a) and size distributions of Y_2O_3:Er^{3+}, Yb^{3+} nanoparticles prepared using the laser ablation method.

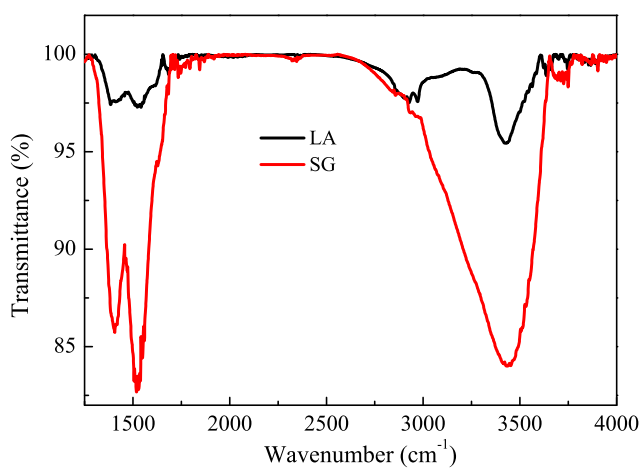

Fig. 2. Fourier transform infra-red (FTIR) spectra of Y_2O_3:Er^{3+}, Yb^{3+} nanoparticles. Measured FTIR spectra of Y_2O_3:Er^{3+}, Yb^{3+} nanoparticles prepared using the laser ablation (LA) and sol–gel (SG) methods.

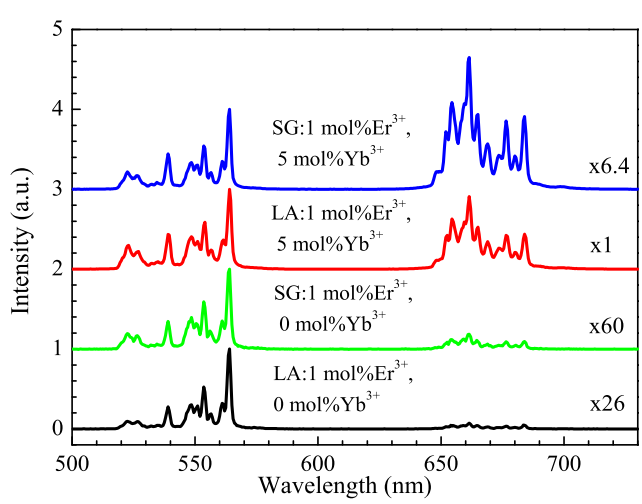

Fig. 3. Upconversion (UC) emission spectra of Y_2O_3:Er^{3+}, Yb^{3+} nanoparticles. UC emission spectra of Y_2O_3:Er^{3+}, Yb^{3+} nanoparticles prepared through the laser ablation (LA) and sol–gel (SG) methods under the 976-nm laser excitation.

upconversion luminescence is explored by the further studies shown below.

3.2. Upconversion emission properties

The UC emission spectra of the Y_2O_3:Er^{3+}, Yb^{3+} nanoparticles prepared through the LA and SG methods are shown in Fig. 3. The green and red UC emissions were observed in the 510–590-nm and 640–690-nm ranges, respectively, which correspond to the respective $^2H_{11/2}/^4S_{3/2} \rightarrow {}^4I_{15/2}$ and $^4F_{9/2} \rightarrow {}^4I_{15/2}$ Er^{3+} ion transitions [20,29,30]. These spectra were normalized to the intensity at 566 nm for ease of comparison. In the Er^{3+}-single-doped samples, green emissions were dominant, while an obvious enhancement in the red emissions could be observed in the Yb^{3+}-co-doped samples. By comparing the UC spectra of the LA and SG samples with identical ion concentrations, one can see that the red emission in the LA samples was reduced. The relative intensities of the red-to-green emission (R/G) were calculated: In the LA samples with 0 and 5 mol% Yb^{3+} ions, R/G was 0.12 and 1.2, respectively; In the SG samples, R/G was 0.27 and 2.49, respectively. Under 976-nm excitation, the upper state, $^4F_{9/2}$, of the red emission can be populated by either nonradiative relaxation (NR II) from $^2H_{11/2}/^4S_{3/2}$, or excited-state absorption (ESA II) or energy transfer (ET III) from $^4I_{13/2}$, as shown in Fig. 4. The appearance of a weak red emission in the

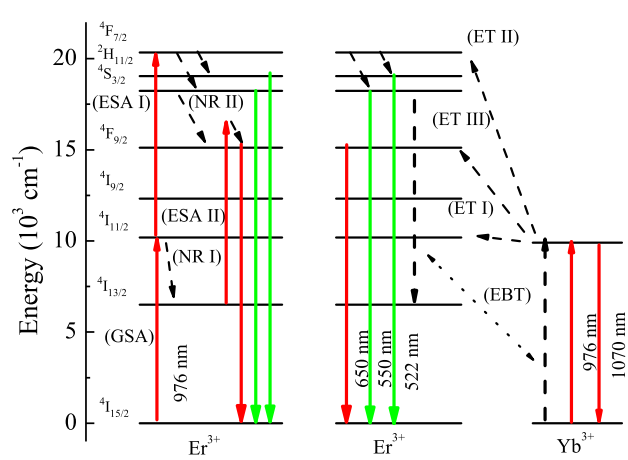

Fig. 4. Energy-level diagram of Er^{3+} and Yb^{3+} ions and proposed upconversion (UC) mechanism for Y_2O_3:Er^{3+}, Yb^{3+} nanocrystals. Energy-level diagram of Er^{3+} and Yb^{3+} ions along with the proposed UC mechanism for Y_2O_3:Er^{3+}, Yb^{3+} nanocrystals under the 976-nm laser excitation.

UC spectra indicates that either the nonradiative relaxation rate or the population of the $^4I_{13/2}$ state was reduced in the LA samples.

To better understand the emission properties of the nanoparticles prepared through the LA method, the UC luminescence intensities of the green and red emissions were measured as a function of the excitation power, as shown in Fig. 5. In the unsaturated condition, the relationship between the excitation power, I_{pump}, and the resulting UC luminescence intensity, I_{UC}, is

$$I_{UC} = a \cdot (I_{pump})^n, \quad (1)$$

where n represents the number of pump photons involved in the UC process and a is a constant. Fig. 5a and b are ln–ln plots of the emission intensities of the LA and SG samples, respectively. It can be observed that, under the same excitation intensity, the nanoparticles prepared through the LA method exhibited higher emission intensity than their counterparts prepared using the SG method, despite having a significantly smaller particle size. The n values (slopes in the figures) were all close to 2, confirming that two-photon processes were involved in populating the $^2H_{11/2}/^4S_{3/2}$ and $^4F_{9/2}$ states. It is worth noting that the n values of the LA samples were lower than those of the SG samples. In fact, n values are typically less than the theoretical values, which can be primarily attributed to competition between the linear decay and UC processes for the depletion of intermediate excited states [31]. Under low pump power excitation, linear decay is dominant and the n value is close to an integer. However, as UC becomes dominant, the n value decreases and even approaches 1, where a "saturation" of the emission intensity is observed. It has been reported that the suppression of energy transfer from Er^{3+} to OH^- groups leads to the enhancement of UC intensity [8]. No clear conclusions on the size-dependent UC emission properties have been obtained in either theoretical studies or experimental investigations. Contrary to quantum dots, the size-dependent luminescence of rare-earth ion doped nanoparticles can't be explained by the theory of quantum confinement of electrons. The active ions are mainly influenced by the local crystal fields and defects absorbed on the particle surface. During the particle size control process, defects were induced by the ligands, which may increase the probability of quenching and nonradiative is increased and subsequently leads to a significant decrease of the UC efficiency. Hence, the size dependent UC luminescence is often accompanied with the change of the FTIR intensity, as well as the number of the groups with large phonon energy [27]. In this work, because of the reduction in the high-energy-phonon-assisted nonradiative relaxation, the linear decay became weak and the UC became increasingly dominant. Hence, the smaller n values also indicate the more effective UC process occurring in the LA samples.

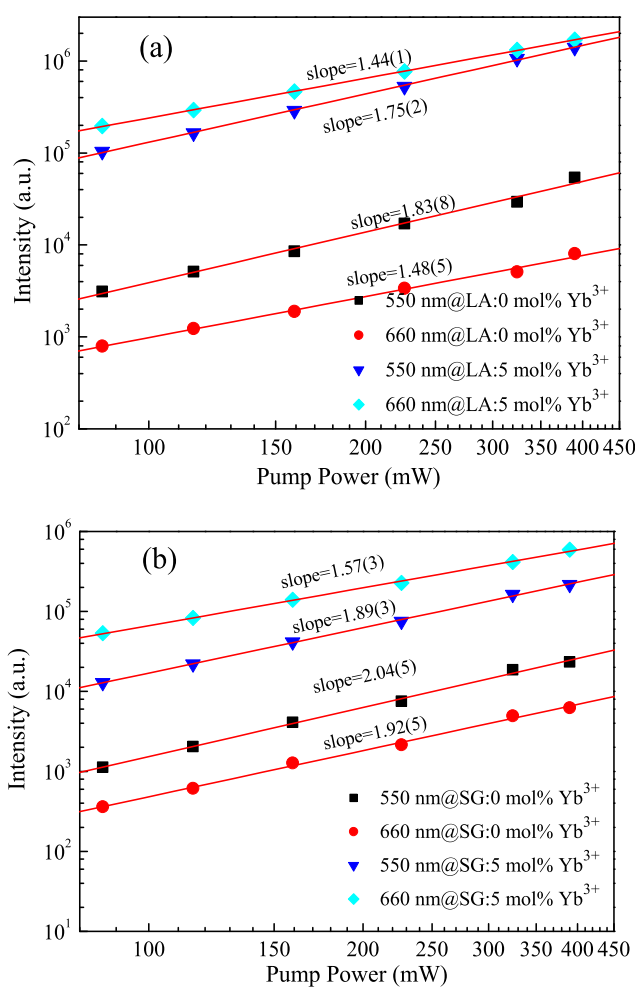

Fig. 5. Green and red upconversion (UC) intensity pump-power dependence in Y_2O_3:Er^{3+}, Yb^{3+} nanoparticles. Pump-power dependence of green and red UC intensities in Y_2O_3:Er^{3+}, Yb^{3+} prepared using the (a) laser ablation (LA) and (b) sol–gel (SG) methods. (For interpretation of the references to color in this figure legend, the reader is referred to the web version of this article.)

3.3. Fluorescence decay time

To confirm the dynamics of the excited states of the rare-earth ions, the luminescence decay times of the UC emissions and the near-infrared DC emission spectra (between 1400 and 1700 nm) from all the samples were measured (see Figs. 6 and 7).

In Fig. 6, the experimental curves for green and red emission display a strong fit to a double exponential function. Generally, the fast-decay component arises from the emitting-level lifetime, and the long component is due to seeding from the intermediate states of $^4I_{11/2}$, $^4I_{13/2}(Er^{3+})$, or $^2F_{5/2}(Yb^{3+})$ [9]. For the Er^{3+}-single-doped samples, the slower green emission component was almost equal to the $^4I_{11/2}$-level lifetime and the slower red emission component almost equated to the $^4I_{13/2}$-level lifetime. This means that the population of the $^4S_{3/2}$ state was primarily related to the excited state absorption (ESA I) from $^4I_{11/2}$, while that of the $^4F_{9/2}$ state was primarily related to ESA II. For the samples co-doped with Yb^{3+} ions, the time constant of the slower component was approximately 0.5 ms, which is 0.5 times the Yb^{3+} ions' $^4F_{5/2}$-level lifetime. It is likely that the populations of the $^4S_{3/2}$ and $^4F_{9/2}$ states were related to the two sequential energy transfers from the excited Yb^{3+} ions. The calculated values of the fast-decay component are listed in the plots. These results indicate that the emitting-level decay times of the LA samples were longer than those of the SG samples, despite having the same concentration. An analysis of the fluorescence decay time shows the influence of the nonradiative relaxation on the dynamics of the UC processes, and it is clear that a limited nonradiative relaxation considerably lengthens the Er^{3+} decay time [32]. The decay time of the emission intensity, τ, can be derived as [33].

$$1/\tau = \sum W_{nr} + \sum A + \sum P_{CR}, \quad (2)$$

where A is the rate of spontaneous emission and P_{CR} is the cross-relaxation rate. Since the samples were doped at the same concentration, A and P_{CR} should be equal, and τ should also be inversely proportional to W_{nr}. Hence, the prolonged decay time confirms the decrease of the nonradiative relaxation rate in the LA

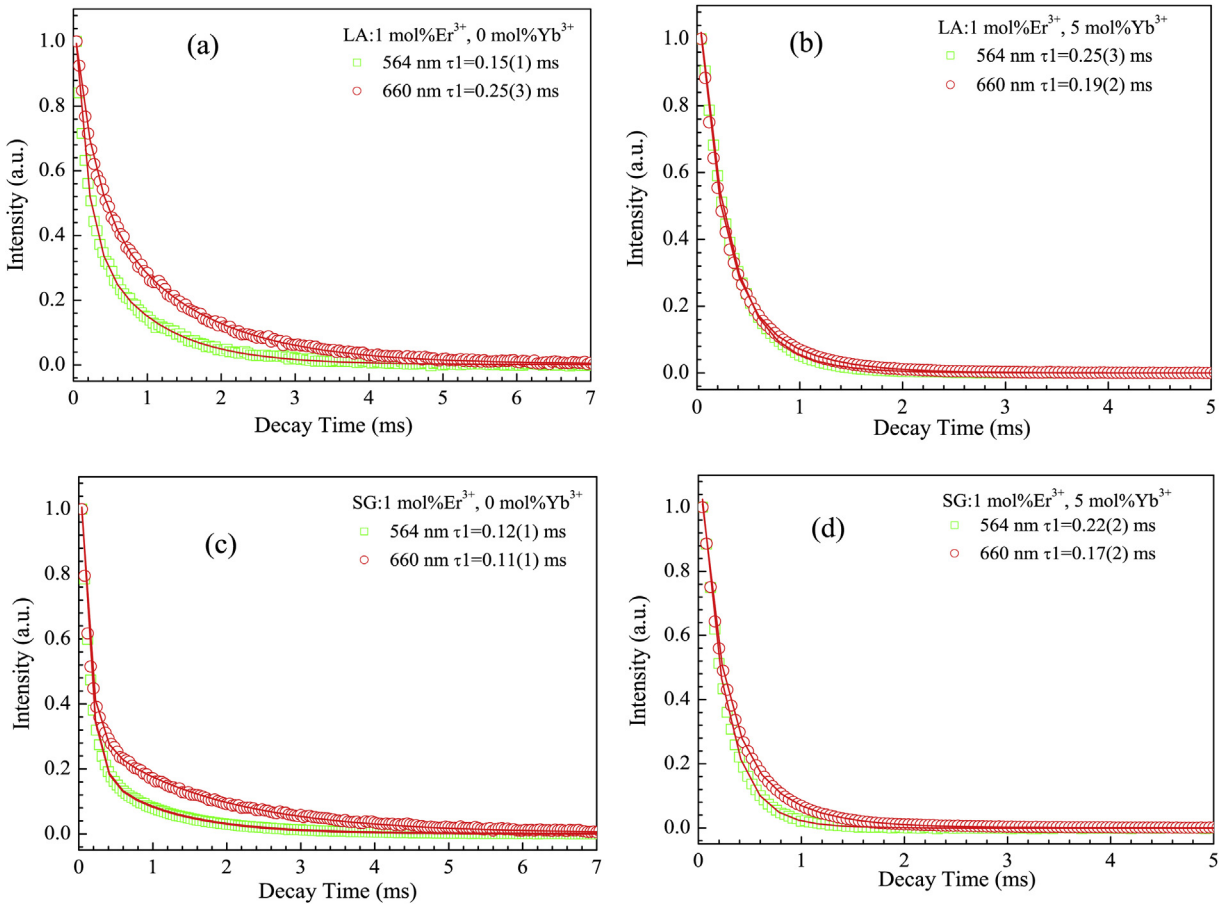

Fig. 6. Emission decay curves in Y_2O_3:Er^{3+}, Yb^{3+} nanoparticles. 564- and 660-nm emission decay curves in Y_2O_3:Er^{3+}, Yb^{3+} nanoparticles prepared using the laser ablation (LA) (top) and sol–gel (SG) (bottom) methods.

samples. This result is consistent with T. López-Luke et al.'s conclusion that enhancement of the emission intensity and decay times can be attributed to a reduction in OH^- and CO_3^{2-} formation, as these groups function as impurities that act to quench luminescence [23].

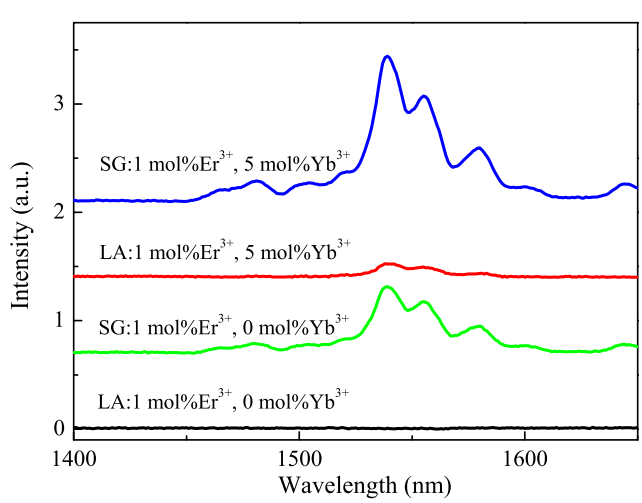

Fig. 7. DC emission spectra of Y_2O_3:Er^{3+}, Yb^{3+} nanoparticles. DC emission spectra of Y_2O_3:Er^{3+}, Yb^{3+} nanoparticles prepared using the laser ablation (LA) and sol–gel (SG) methods under the 976-nm laser excitation.

3.4. Near infrared downconversion properties

Fig. 7 shows the near-infrared DC emission spectra of the Y_2O_3:Er^{3+}, Yb^{3+} nanoparticles prepared using the LA and SG methods under 976-nm diode laser excitation. The emission band centered at 1550 nm was assigned to the $^4I_{13/2}(Er^{3+}) \rightarrow {}^4I_{15/2}(Er^{3+})$ transition [10,34]. In the LA samples, the 1550-nm intensity was very low, while no 1550-nm emission could be observed for the Er^{3+}-single-doped sample. Although codoping with Yb^{3+} ions rendered the 1550-nm emission slightly visible, the intensity was still significantly weaker than that of the SG samples. To the best of our knowledge, few authors have reported such a significantly suppressed near-infrared emission of Er^{3+} ions under 976-nm laser excitation. As for the 1550-nm emission, the $^4I_{13/2}$ emitting state cannot be directly populated (excited) by a 976-nm photon, and the dominant population processes are described as follows: The Er^{3+} ions are first populated into the $^4I_{11/2}$ state by ground-state absorption (GSA) or energy transfer from excited Yb^{3+} ions (ET I). Then, some of the excited ions decay from the $^4I_{11/2}$ excited state to a long-lived $^4I_{13/2}$ state through the nonradiative relaxation (NR I) process, $^4I_{11/2}(Er^{3+}) \rightarrow {}^4I_{13/2}(Er^{3+})$. For high Yb^{3+} concentration, the energy-back transfer (EBT) process, $^4S_{3/2}(Er^{3+}) + {}^2F_{7/2}(Yb^{3+}) \rightarrow {}^4I_{13/2}(Er^{3+}) + {}^2F_{5/2}(Yb^{3+})$, becomes more prominent [7,35]. This process is also responsible for the population of the $^4I_{13/2}$ state. Although doping with Yb^{3+} ions increases the population of the $^4I_{13/2}$ state through EBT, the 1550-nm emission in the LA sample is still significantly weaker than that of the SG samples. This implies that the NR I process is the most effective channel for populating

the $^4I_{13/2}$ state, and causes the SG samples to present intense 1550-nm emission. Considering that the cutoff phonon energy ($\hbar\omega$) for Y_2O_3 is ~560 cm^{-1} and an energy gap of ΔE ~3200 cm^{-1} exists between the $^4I_{11/2}$ and $^4I_{13/2}$ Er^{3+} states, the estimated number of phonons ($P = \Delta E/\hbar\omega$) emitted in the NR I process is at least six. The relationship between the nonradiative relaxation rate, W_{nr}, and the number of phonons, P, can be calculated as

$$W_{nr} = C \cdot \exp(-a \cdot P), \quad (3)$$

where C and a are positive constants [33]. This means that W_{nr} should be lower for the samples with smaller $\hbar\omega$. Compared to the FTIR spectra shown in Fig. 2, significantly weaker absorption can be observed at approximately 3500 and 1500 cm^{-1} for the LA samples, which correspond to vibrations from the OH^- and CO_3^{2-} groups, respectively. Thus, the LA samples possess few high-energy phonons and must rely on the intrinsic yttrium phonon solely. The elimination of these high-energy phonons significantly reduces W_{nr} and almost suppresses NR I. This leads to a substantial decrease in the Er^{3+} ion population of $^4I_{13/2}$ and, thus, 1550-nm emission in the LA samples.

Based on the analysis above, it can be concluded that reduction of the OH^- and CO_3^{2-} groups causes the LA samples to present longer UC emission decay times and highly suppressed 1550-nm emission. These results are all attributed to the elimination of nonradiative relaxation assisted by high-energy phonons. Furthermore, the suppression of the population of the $^4I_{13/2}$ state leads to a decrease in the relative intensities of the red-to-green emission [14,36].

4. Conclusions

Er^{3+}- and Yb^{3+}-doped Y_2O_3 nanoparticles were directly synthesized by femtosecond-pulse laser ablation on a corresponding oxide mixture. Nanoparticles with sizes significantly less than 50 nm were obtained and the FTIR spectra indicated a decrease in the number of carbonate and hydroxyl groups. The emission properties of the nanoparticles prepared using laser ablation were then studied in the visible and infrared regions, and it was found that these nanoparticles exhibited small relative red-to-green emission intensities. Overall, the observed higher upconversion intensity and the decreasing power dependence of the emission intensity indicate that the upconversion process is more efficient in the laser-ablated samples. The long decay time of the upconversion emission and almost suppressed 1550-nm emission can be attributed to a reduction of the nonradiative relaxation induced by high-energy phonons. As the emission mechanism in these nanoparticles is strongly dependent on the concentration of high-phonon-energy groups, preventing the appearance of such groups in the preparation process can reduce non-radiative loss and lead to improvements in the upconversion emission properties. Thus, femtosecond-pulse laser ablation is a promising method for preparing higher-efficiency upconversion nanoparticles.

Acknowledgments

This work was supported by the National Natural Science Foundation of China under Grant no. 61308050 and Fundamental Research Project of Chinese State Key Laboratory of Laser Interaction with Matter under Grant no. SKLLIM 1210-01.

References

[1] G.S. Yi, H.C. Lu, S.Y. Zhao, G. Yue, W.J. Yang, D.P. Chen, L.H. Guo, Synthesis, characterization, and biological application of size-controlled nanocrystalline $NaYF_4$:Yb,Er infrared-to-visible up-conversion phosphors, Nano Lett. 4 (2004) 2191–2196.
[2] L. Wang, R. Yan, Z. Huo, L. Wang, J. Zeng, J. Bao, X. Wang, Q. Peng, Y. Li, Fluorescence resonant energy transfer biosensor based on upconversion-luminescent nanoparticles, Angew. Chem. Int. Ed. 44 (2005) 6054–6057.
[3] J.H. Zeng, J. Su, Z.H. Li, R.X. Yan, Y.D. Li, Synthesis and upconversion luminescence of hexagonal-phase $NaYF_4$:Yb^{3+}, Er^{3+}, phosphors of controlled size and morphology, Adv. Mater. 17 (2005) 2119–2123.
[4] F. Wang, D. Banerjee, Y. Liu, X. Chen, X. Liu, Upconversion nanoparticles in biological labeling, imaging, and therapy, Analyst 135 (2010) 1839–1854.
[5] X.M. Li, F. Zhang, D.Y. Zhao, Lab on upconversion nanoparticles: optical properties and applications engineering via designed nanostructure, Chem. Soc. Rev. 44 (2015) 1346–1378.
[6] W. Zheng, P. Huang, D.T. Tu, E. Ma, H.M. Zhu, X.Y. Chen, Lanthanide-doped upconversion nano-bioprobes: electronic structures, optical properties, and biodetection, Chem. Soc. Rev. 44 (2015) 1379–1415.
[7] F. Wang, F. Song, G. Zhang, Y. Han, Q. Li, C. Ming, J. Tian, Upconversion and pump saturation mechanisms in Er^{3+}/Yb^{3+} co-doped $Y_2Ti_2O_7$ nanocrystals, J. Appl. Phys. 115 (2014), 134310-1–134310-7.
[8] L. Liu, H. Jiang, Y. Chen, X. Zhang, Z. Zhang, Y. Wang, Power dependence of upconversion luminescence of Er^{3+} doped Yttria nanocrystals and their bulk counterpart, J. Lumin. 143 (2013) 423–431.
[9] H. Liang, G. Chen, H. Liu, Z. Zhang, Ultraviolet upconversion luminescence enhancement in Yb^{3+}/Er^{3+}-codoped Y_2O_3 nanocrystals induced by tridoping with Li^+ ions, J. Lumin. 129 (2009) 197–202.
[10] H. Desirena, L.A. Diaz-Torres, R.A. Rodríguez, O. Meza, P. Salas, C. Angeles-Chávez, E.H. Tobar, J. Castañeda-Contreras, E. De la Rosa, Photoluminescence characterization of porous YAG:Yb^{3+}-Er^{3+} nanoparticles, J. Lumin. 153 (2014) 21–28.
[11] Y.S. Zhu, W. Xu, G.Q. Li, S.B. Cui, X.Y. Liu, H.W. Song, Plasmonic enhancement of the upconversion fluorescence in YVO_4:Yb^{3+}, Er^{3+} nanocrystals based on the porous Ag film, Nanotechnology 26 (2015), 145602-1–145602-8.
[12] F. Huang, Y. Gao, J.C. Zhou, J. Xu, Y.S. Wang, Yb^{3+}/Er^{3+} co-doped $CaMoO_4$: a promising green upconversion phosphor for optical temperature sensing, J. Alloy. Compd. 639 (2015) 325–329.
[13] M. Liu, S.W. Wang, J. Zhang, L.Q. An, L.D. Chen, Dominant red emission ($^4F_{9/2} \rightarrow {}^4I_{15/2}$) via upconversion in YAG ($Y_3Al_5O_{12}$):Yb^{3+}, Er^{3+} nanopowders, Opt. Mater. 29 (2007) 1352–1357.
[14] B. Xue, J. Sun, Synthesis and tuning orange to green up-conversion color in Y_6WO_{12}:Er/Yb phosphor, Opt. Mater. 36 (2013) 278–282.
[15] Q. Lu, Y. Hou, A. Tang, Y. Lu, L. Lv, F. Teng, Controlled synthesis and defect dependent upconversion luminescence of Y_2O_3:Yb,Er nanoparticles, J. Appl. Phys. 115 (2014), 074309-1–074309-4.
[16] V. Singh, V.K. Rai, K. Al-Shamery, M. Haase, S.H. Kim, NIR to visible frequency upconversion in Er^{3+} and Yb^{3+} codoped ZrO_2 phosphor, Appl. Phys. A 113 (2013) 747–753.
[17] R.S. Yadav, R.K. Verma, A. Bahadur, S.B. Rai, Infrared to infrared upconversion emission in Pr^{3+}/Yb^{3+} co-doped La_2O_3 and $La(OH)_3$ nano-phosphors: a comparative study, Spectrochim. Acta A 142 (2015) 324–330.
[18] B. Xue, J.Y. Sun, Upconversion emission properties and tunable morphologies of Y_6WO_{12}:Yb^{3+}/Er^{3+} phosphor, Infrared Phys. Technol. 62 (2014) 45–49.
[19] X. Yu, M. Gao, J. Li, L. Duan, N. Cao, Z. Jiang, A. Hao, P. Zhao, J. Fan, Near infrared to visible upconversion emission in Er^{3+}/Yb^{3+} co-doped $NaGd(WO_4)_2$ nanoparticles obtained by hydrothermal method, J. Lumin. 154 (2014) 111–115.
[20] R. Adhikari, B. Joshi, R. Narrog-García, E. De la Rosa, S.W. Lee, Microwave hydrothermal synthesis and infrared to visible upconversion luminescence of Er^{3+}/Yb^{3+} co-doped bismuth molybdate nanopowder, J. Lumin. 145 (2014) 866–871.
[21] Y.X. Liu, M.H. Sun, Y. Liu, G.Q. Chen, X. Zhang, Effects of aging time on phase, morphology, and luminescence by two-photon processes of $BiPO_4$:Er^{3+}, Yb^{3+} in the solvothermal synthesis, Opt. Mater. 45 (2015) 32–36.
[22] H. Yu, W.B. Cao, Q.M. Huang, E. Ma, X.Q. Zhang, J.C. Yu, Upcoversion performance improvement of $NaYF_4$:Yb, Er by Sn codoping: enhanced emission intensity and reduced decay time, J. Solid State Chem. 207 (2013) 170–177.
[23] T. López-Luke, E. De la Rosa, I.C. Villalobos, R.A. Rodriguez, C. Ángles-Chávez, P. Salas, D.A. Wheeler, J.Z. Zhang, Improving pure red upconversion emission of Co-doped Y_2O_3:Yb^{3+}-Er^{3+} nanocrystals with a combination of sodium sulfide and surfactant pluronic-F127, J. Lumin. 145 (2014) 292–298.
[24] C.B. Zheng, Y.Q. Xia, F. Qin, Y. Yua, J.P. Miao, Z.G. Zhang, W.W. Cao, Femtosecond pulsed laser induced synthesis of ultrafine Y_2O_3:Pr, Yb nanoparticles with improved upconversion efficiency, Chem. Phys. Lett. 496 (2010) 316–320.
[25] G.Y. Chen, Y. Liu, Z.G. Zhang, B. Aghahadi, G. Somesfalean, Q. Sun, F.P. Wang, Four-photon upconversion induced by infrared diode laser excitation in rare-earth-ion-doped Y_2O_3 nanocrystals, Chem. Phys. Lett. 448 (2007) 127–131.
[26] K. Fujii, Y. Kitamoto, M. Hara, O. Odawara, H. Wada, Optical properties of silica-coated Y_2O_3:Er,Yb nanoparticles in the presence of polyvinylpyrrolidone, J. Lumin. 156 (2014) 8–15.
[27] X.J. Xue, S. Uechi, R.N. Tiwari, Z.C. Duan, M.S. Liao, M. Yoshimura, T. Suzuki, Y. Ohishi, Size-dependent upconversion luminescence and quenching mechanism of LiYF4:Er^{3+}/Yb^{3+} nanocrystals with oleate ligand absorbed, Opt. Mater. Express 3 (2013) 989–999.
[28] R.V. Perrella, D.P. dos Santos, G.Y. Poirier, M.S. Góes, S.J.L. Ribeiro, M.A. Schiavon, J.L. Ferrari, Er^{3+}-doped Y_2O_3 obtained by polymeric precursor: synthesis, structure and upconversion emission properties, J. Lumin. 149 (2014) 333–340.

[29] W. Gao, H. Zheng, E. He, Y. Lu, F. Gao, Luminescence investigation of Yb^{3+}/Er^{3+} codoped single $LiYF_4$ microparticle, J. Lumin. 152 (2014) 44–48.
[30] L. Strizik, J. Zhang, T. Wagner, J. Oswald, T. Kohoutek, B.M. Walsh, J. Prikryl, R. Svoboda, C. Liu, B. Frumarova, M. Frumar, M. Pavlista, W.J. Park, J. Heo, Green, red and near-infrared photon up-conversion in Ga-Ge-Sb-S:Er^{3+} amorphous chalcogenides, J. Lumin. 147 (2014) 209–215.
[31] M. Pollnau, D.R. Gamelin, S.R. Lüthi, H.U. Güdel, M.P. Hehlen, Dependence of upconversion luminescence in lanthanide and transition-metal-ion systems, Phys. Rev. B 61 (2000) 3337–3346.
[32] H. Liang, Y. Zheng, G. Chen, L. Wu, Z. Zhang, W. Cao, Enhancement of upconversion luminescence of Y_2O_3:Er^{3+} nanocrystals by codoping Li^{+}-$Zn2^{+}$, J. Alloy. Compd. 509 (2011) 409–413.
[33] A. Patra, Effect of crystal structure and concentration on luminescence in Er^{3+}:ZrO_2 nanocrystals, Chem. Phys. Lett. 387 (2004) 35–39.
[34] A. Miguel, M.A. Arriandiaga, R. Morea, J. Fernandez, J. Gonzalo, R. Balda, Down- and up-conversion emissions in Er^{3+}-Yb^{3+} codoped TeO_2-ZnO-ZnF_2 glasses, J. Lumin. 158 (2015) 142–148.
[35] L. Shi, Q. Shen, Z. Qiu, Concentration-dependent upconversion emission in Er-doped and Er/Yb-codoped $LiTaO_3$ polycrystals, J. Lumin. 148 (2014) 94–97.
[36] H. Wu, Z. Yang, J. Liao, S. Lai, J. Qiu, Z. Song, Y. Yang, D. Zhou, Z. Yin, Upconversion luminescence properties of three-dimensional ordered macroporous CeO_2:Er^{3+}, Yb^{3+}, J. Alloy. Compd. 586 (2014) 485–487.